1

Recent Progress in Theory of Thermoelectric Effect: Focusing on Types I, II, and III Dirac Systems and Film-substrate Systems

Hiroyasu Matsuura[1] *and Tomonari Mizoguchi*[2]

[1] *National Institute of Advanced Industrial Science and Technology (AIST), Tsukuba, Ibaraki, Japan*
[2] *Department of Physics, Institute of Pure and Applied Sciences, University of Tsukuba, Tsukuba, Ibaraki, Japan*

1.1 Introduction

The thermoelectric effect, which is a phenomenon converting the temperature gradient to the electric voltage, has been used in special applications such as the exploration satellites, while recently the thermoelectric effect has been focused on not only the special applications but also the green power generation and the power supply for the Internet of Things society [1]. The conversion efficiency of the thermoelectric effect (η) is given by $\eta = \eta_c \dfrac{\sqrt{1+ZT}-1}{\sqrt{1+ZT}+T_c/T_h}$, where η_c and ZT indicate the Carnot efficiency and the dimensionless figure of merit, respectively, and T_c and T_h are the temperature of the cold and hot sides. ZT is mathematically given by $ZT = S^2\sigma T/\kappa$, where S, σ, κ, and T are Seebeck coefficient, electric conductivity, thermal conductivity, and temperature, respectively. Since these parameters are material parameters, for the innovation of thermoelectric materials with high efficiency, the precise control of these parameters is required. Unique electronic states such as Dirac electrons, which have been intensively studied in the field of solid-state physics, are of interest [2].

Another method to increase efficiency is to utilize composite systems consisting of several materials. The film-substrate system is a typical example of composite systems. The Seebeck effect in the film-substrate system has been studied in detail [3–6], while the transverse thermoelectric effect, such as the anomalous Nernst effect in the film-substrate system, has been focused on recently, because a huge increase of the anomalous Nernst effect was observed in Fe–Ga alloy on silicon substrate [6].

To analyze the thermoelectric effect theoretically, phenomenological methods such as the Boltzmann equation have been used, while, recently, the microscopic method based on the formalism by Kubo and Luttinger, which can treat the quantum effect exactly, has developed [7–9]. Therefore, first, we introduce the microscopic method based on the Kubo–Luttinger formalism briefly. Then, we apply this method to the thermoelectric effect of type I, II, and III Dirac electrons, which is one of the unique electronic states in solids [10]. Next, we introduce the recent development of film-substrate systems and describe theoretical methods to analyze the thermoelectric effect in film-substrate systems [11].

1.2 Linear Response Theory Based on Kubo–Luttinger and Application to Dirac-electron Systems

1.2.1 Liner Response

When an external electric filed (E) is applied to solids, an electric current is generated. Similarly, applying the temperature gradient (∇T) generates the heat current. These are called Ohm's law and Fourier's law, respectively. On the other hand, the correlated effect between the electric field and the heat current or that between the temperature gradient and the electric current is also known. In the region of the linear response, these phenomena are formally given by

$$J_e = L_{11}E + L_{12}\left(-\frac{\nabla T}{T}\right), \tag{1.1}$$

$$J_Q = L_{21}E + L_{22}\left(-\frac{\nabla T}{T}\right), \tag{1.2}$$

where J_e and J_Q are the densities of the electric current and the heat current, respectively, L_{ij} denote the coefficients of the linear response, and especially L_{11} is called the electric conductivity.

When the temperature gradient is applied to solids, the diffusion of electrons is generated, and, finally, the internal electric field is generated by the diffusion that becomes balanced with the temperature gradient. The ratio between the internal electric field and temperature gradient corresponds to the Seebeck coefficient. Using Eq. (1.1) with the condition of $J_e = 0$, the Seebeck coefficient is given by

$$S = \frac{E}{\nabla T} = \frac{L_{12}}{TL_{11}}. \tag{1.3}$$

Since the Seebeck coefficient is expressed by the coefficients of linear response, the precise estimation of these coefficients is required in theoretical calculations.

1.2.2 Framework of Thermoelectric Theory Based on Kubo–Luttinger Formalism

Electric transport due to the electric field is calculated microscopically by the Kubo formula (i.e., the linear response theory) [7]. On the other hand, the linear response theory of temperature gradient is qualitatively different from that of the electric field. This is because the electric field is a mechanical external field, while the temperature gradient is a statical quantity. Thus, the linear response of the temperature gradient had been difficult to deal with. Luttinger suggested the linear response theory to treat the temperature gradient, using the relationship between the temperature gradient and gravitational potential [8].

Recently, the thermoelectric microscopic theory based on Kubo–Luttinger formalism has been extended [9]. In this section, we introduce the recent progress of the Kubo–Luttinger formalism briefly.

In the Kubo–Luttinger formalism, the thermoelectric effect (precisely speaking L_{12}) is derived based on the heat currents generated depending on the Hamiltonians. Figure 1.1 shows the schematic picture of the Hamiltonians and heat currents generated from each term of the Hamiltonian. Generally, the thermoelectric effects can be divided into three kinds of effects. One is a diffusive thermoelectric effect, as shown in Figure 1.1. The effect is formally given by

$$L_{11} = \int d\epsilon \left(-\frac{\partial f(\epsilon)}{\partial \epsilon}\right) \sigma(\epsilon, T), \tag{1.4}$$

$$L_{12} = \frac{1}{e} \int d\epsilon \left(-\frac{\partial f(\epsilon)}{\partial \epsilon}\right) (\epsilon - \mu)\, \sigma(\epsilon, T), \tag{1.5}$$

where $f(\epsilon)$, $\sigma(\epsilon, T)$, and μ indicate the Fermi distribution function, spectral function, and the chemical potential, respectively. $e\,(<0)$ is the charge of an electron. Since this equation was first derived by Sommerfeld–Bethe [12], Eq. (1.5) is called the Sommerfeld–Bethe (SB) relation [9]. By using the Sommerfeld expansion in metals at low temperatures, we can derive the Mott formula

$$S = \frac{\pi^2}{3} \frac{k_B^2 T}{e} \frac{\partial ln\sigma(\epsilon_F, 0)}{\partial \epsilon_F}. \tag{1.6}$$

The theory of the thermoelectric effect based on the SB relation has been extended to the analysis of many materials [10, 13–22].

A second thermoelectric effect is a phonon-assisted effect. Applying the temperature gradient to solids, the heat current of phonons is generated. The thermoelectric

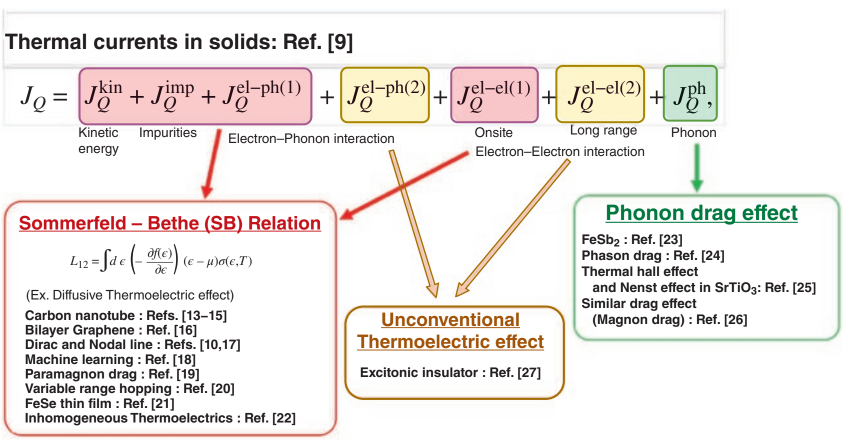

Figure 1.1 Schematic picture of framework and applications of thermoelectric theory based on the Kubo–Luttinger formula.

effect occurs by generating an electric flow through the electron–phonon interaction. This effect is called the phonon drag effect, and the microscopic theory of the drag effect based on Kubo–Luttinger formalism was performed [23–26].

Finally, we describe the thermoelectric effects due to the thermal currents deriving from the many-body effects such as electron–electron interaction and electron–phonon interaction. This thermoelectric effect has not been studied in detail; therefore, this effect is expected to become an unconventional thermoelectric effect [27].

1.2.3 Application to Dirac-electron Systems

Materials that host electrons behaving as relativistic particles which appear in the vicinity of the Fermi surfaces due to a characteristic band dispersion are called Dirac-electron systems. For decades, the Dirac electrons have been known to be realized in bismuth single crystals [28]. Bismuth is a bulk material, and it has a small but finite band gap at the L point. Recently, it was revealed that Dirac electrons also appear in two-dimensional materials such as graphene [29] and quasi-two-dimensional systems (materials have a three-dimensional structure, but the electron conductivity is strong only in the plane) such as an organic conductor α-(BEDT-TTF)$_2$I$_3$ [30]. In these materials, the band gap (ideally) closes; that is, the conduction and the valence bands touch at some points in the momentum space. Such systems are called the massless Dirac electrons, and the band-touching points are called the Dirac points. Particularly in two dimensions, when drawing the dispersion relation as a function of two-dimensional momentum $\left[\boldsymbol{k} = (k_x, k_y)\right]$, its shape is two cones touching at their apexes. Thus, the spectrum around the Dirac points is called the Dirac cones. Here, we introduce an example of a microscopic study of the thermoelectric effect in two-dimensional Dirac electrons [10].

One of the characteristics of Dirac electrons in solids is that there can be anisotropic dispersion. Dirac cones are classified into three types according to the shape of the equienergy line around the Dirac point, which is determined by the degree of tilting. To see this, let us consider the minimal model describing the tilted massless Dirac cones, whose Hamiltonian is given as a 2×2 matrix as a function of $\boldsymbol{k}$, as

$$H(\boldsymbol{k}) = \lambda \hbar v_{\mathrm{F}} k_x \sigma_0 + \hbar v_{\mathrm{F}} \boldsymbol{k} \cdot \boldsymbol{\sigma}. \tag{1.7}$$

Here, $\boldsymbol{\sigma} = (\sigma_x, \sigma_y, \sigma_z)$ with $\sigma_x = \begin{pmatrix} 0 & 1 \\ 1 & 0 \end{pmatrix}$, $\sigma_y = \begin{pmatrix} 0 & -i \\ i & 0 \end{pmatrix}$, and $\sigma_z = \begin{pmatrix} 1 & 0 \\ 0 & -1 \end{pmatrix}$ are called the Pauli matrices, and $\sigma_0 = \begin{pmatrix} 1 & 0 \\ 0 & 1 \end{pmatrix}$ is the 2×2 identity matrix. Diagonalizing $H(\boldsymbol{k})$, we obtain the dispersion relation, $\varepsilon_{\boldsymbol{k}}^{\pm} = \hbar v_{\mathrm{F}} (\lambda k_x \pm k)$ with $k = \sqrt{k_x^2 + k_y^2}$. The superscript $\pm$ is the band index, where $+$ denotes the upper band and $-$ denotes the lower band. Figure 1.2 is the schematic figure of the dispersion relation for several values of λ. For $\lambda < 1$, the tilting is small enough, and the equienergy line around the

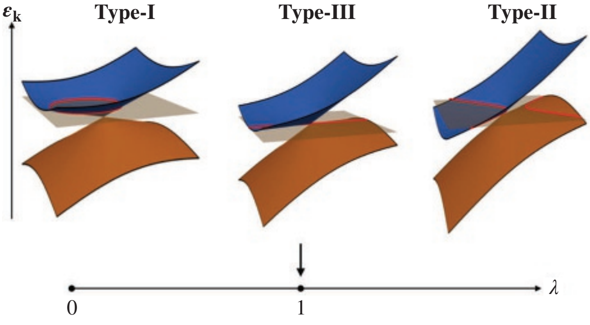

Figure 1.2 Schematic figure of the dispersion relation of the minimal Dirac Hamiltonian with tilted cones in Eq. (1.7).

Dirac point has an elliptical shape. This type of Dirac cone is called the type I Dirac cone, and graphene and α-(BEDT-TTF)$_2$I$_3$ belong to this class. On the other hand, for $\lambda > 1$, the tilting is large enough, and the shape of the equienergy line turns to the hyperbola. This type of Dirac cone is called the type II Dirac cone. The type III Dirac cone is the critical case (i.e., the transition point) between these two types. At the zero energy, the equienergy line is the straight line along a certain direction; that is, the dispersion is completely flat along the direction of tilting (i.e., the k_x direction in this model). Among these three types, when the Fermi level is at zero energy, type I is the gapless semiconductor, and the density of state at the Fermi level vanishes, while the other two types have a finite density of state.

The minimal model of Eq. (1.7) has been used to study the physical properties, such as the transport phenomena and electric/magnetic responses, of the Dirac-electron systems. However, in this model, for types II and III, the Fermi surface (or the line for the two-dimensional systems) extends to infinitely far away from the Dirac point. On the other hand, in the actual solid-state systems, the momentum space is bounded by the Brillouin zone, and the Fermi surface has to have a closed shape. Therefore, in the theoretical studies, tight-binding-type models, where the effect of the Brillouin zone is properly taken into account, are often used. Here, we argue one of such examples [31]. To be specific, we argue the two-orbital model on a square lattice, whose Hamiltonian in the momentum space is given as

$$H(\boldsymbol{k}) = d_{\boldsymbol{k}}^0 \sigma_0 + \boldsymbol{d}_{\boldsymbol{k}} \cdot \boldsymbol{\sigma}, \tag{1.8}$$

where $d_{\boldsymbol{k}}^0 = 2\lambda t' \left(\cos k_x a_0 - \cos k_y a_0\right)$, $d_{\boldsymbol{k}}^x = 2t' \left(\cos k_x a_0 - \cos k_y a_0\right)$, $d_{\boldsymbol{k}}^y = 0$, and $d_{\boldsymbol{k}}^z = 2t \left(\cos k_x a_0 + \cos k_y a_0\right)$. Dirac points appear at the momentum where $d_{\boldsymbol{k}}^x = d_{\boldsymbol{k}}^z = 0$; that is, $\boldsymbol{k} = \left(\pm\frac{\pi}{2a_0}, \pm\frac{\pi}{2a_0}\right)$,with all combinations of signs being allowed. a_0 stands for the lattice constant. The parameters t and $t'$are the hopping parameters having the dimension of the energy, while λ in $d_{\boldsymbol{k}}^0$ is the dimensionless parameters controlling the tilting. Figure 1.3 shows the dispersion relations for the lattice model, where we see that the type I, II, and II Dirac cones are realized at $\varepsilon_{\boldsymbol{k}} = 0$ for $\lambda < 1$, $\lambda > 1$, and $\lambda = 1$, respectively. In this study, as typical values for electrons in solids, the tight-binding parameters are set as $(t, t' = -1\,\text{eV}, -0.3\,\text{eV})$.

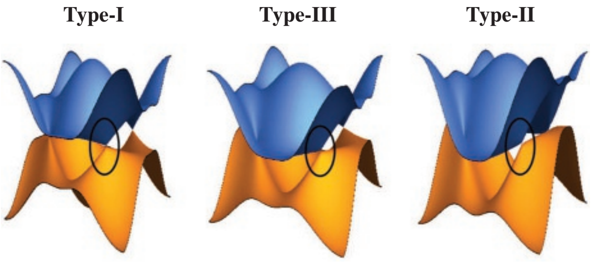

Figure 1.3 Schematic figure of the dispersion relation of the tight-binding model in Eq. (1.8). Black ellipses denote one of four Dirac cones.

In the following, we present the results of the thermoelectric transport based on the Kubo–Luttinger formalism [7, 8]. To be specific, we consider the quasi-two-dimensional system; that is, the layers, whose areas are A and each of which hosts the electrons described by the Hamiltonian of Eq. (1.8), are stacked independently with the interlayer spacing $d_0 = 10$ Å. The spin degrees of freedom are neglected. Under this setup, the spectral conductivity $\sigma(\epsilon)$ is calculated by using the following formula,

$$\sigma(\epsilon) = \frac{\hbar e^2}{2\pi A d_0} \sum_{\boldsymbol{k}} \mathrm{Tr}\left\{G^{(R)}(\boldsymbol{k},\epsilon)\, v_x(\boldsymbol{k})\, G^{(A)}(\boldsymbol{k},\epsilon)\, v_x(\boldsymbol{k}) - Re\left[G^{(R)}(\boldsymbol{k},\epsilon)\, v_x(\boldsymbol{k})\, G^{(R)}(\boldsymbol{k},\epsilon)\, v_x(\boldsymbol{k})\right]\right\} \tag{1.9}$$

Here $G^{(R)}(\boldsymbol{k},\epsilon) = [\epsilon + i\Gamma - H(\boldsymbol{k})]^{-1}$ and $G^{(A)}(\boldsymbol{k},\epsilon) = [\epsilon - i\Gamma - H(\boldsymbol{k})]^{-1}$ are the retarded and advanced Green's functions, respectively, and $v_x(\boldsymbol{k}) = \frac{1}{\hbar}\frac{\partial H(\boldsymbol{k})}{\partial k_x}$ is the velocity operator in the x-direction, which is the direction of the applied electric field and the temperature gradient. Γ denotes the quasi-particle damping rate arising from the impurity scattering, which is approximated as a constant. This approximation is called the relaxation time approximation. For the numerical calculations, Γ is set to be 0.02 eV.

Figure 1.4 shows the spectral conductivity for three values of λ. We see that the conductivity exhibits a dip for the type I and III Dirac cones, whereas it exhibits a peak for the type II cone. This qualitative difference is clearly manifested in the thermoelectric response.

To estimate ZT, assume that the thermal conductivity κ consists only of the electronic contribution. In that case, κ is estimated

$$\kappa = \frac{1}{T}\left(L_{22} - \frac{L_{12}^2}{L_{11}}\right), \tag{1.10}$$

with

$$L_{22} = \frac{1}{e^2}\int d\epsilon \left(-\frac{\partial f(\epsilon)}{\partial \epsilon}\right)(\epsilon-\mu)^2 \sigma(\epsilon, T). \tag{1.11}$$

As our interest is in the thermoelectric responses in the vicinity of the transition point from types I to II, we consider values of λ; namely, $\lambda = 0.95$ (type I), $\lambda = 1$ (type III), and $\lambda = 1.5$ (type II). Figure 1.5 shows the temperature dependence of

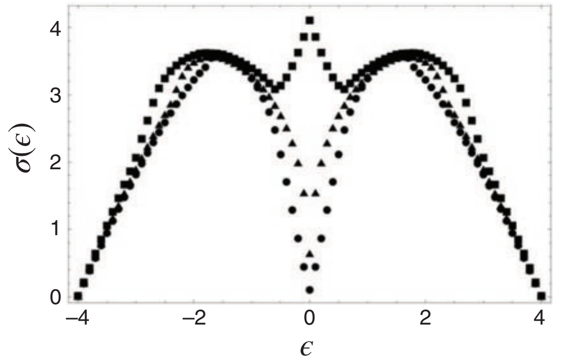

Figure 1.4 Spectral conductivity for the lattice model. The dots, triangles, and squares are for $\lambda = 0.5$ (type I), $\lambda = 1$ (type III), and $\lambda = 1.5$ (type II), respectively. $\sigma(\epsilon)$ is in the unit of $10^6/\Omega$ m, and ϵ is in the unit of eV.

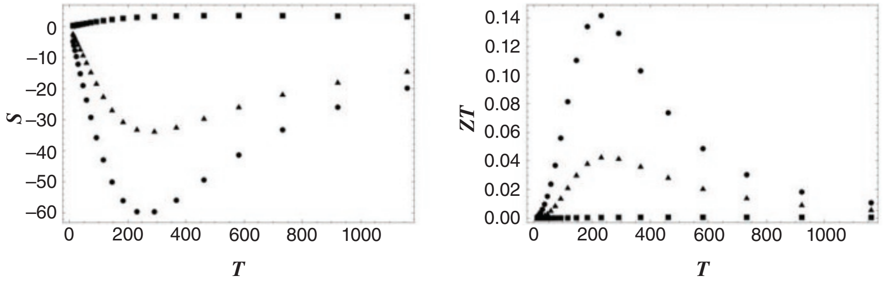

Figure 1.5 Seebeck coefficient (left) and the dimensionless figure of merit (right) as a function of temperature. The dots, triangles, and squares are for $\lambda = 0.95$ (type I), $\lambda = 1$ (type III), and $\lambda = 1.5$ (type II), respectively. S is in the unit of μV/K, and T is in the unit of K.

S and ZT. Here, the chemical potential μ is set to be 0.05 eV. The type I and III cases have noticeably large values of $|S|$ and ZT compared with the type II case, which indicates that the dip of the spectral conductivity around the Dirac points is the key element to obtain the large thermoelectric response. It is also seen that $\lambda = 1$ (type III) does not give the maximal thermoelectric response. In fact, within our numerical investigations, the maximal values of $|S|$ and ZT are obtained for $\mu = 0.05$ eV and $\lambda = 0.89$, and the values are $|S| \sim 70$ μV/K and $ZT \sim 0.18$. These results indicate that the fine-tuning of the electronic structure (i.e., the tilting of the cone in this case) and the chemical potential is needed to optimize the thermoelectric response.

In Figure 1.5, we also see that the overall temperature dependences of S and ZT for the type I and III Dirac cones are very similar. In particular, the peak positions of these two types are almost the same. We discuss the origin of this similarity with respect to the approximated forms of the spectral conductivity. A method of estimating the thermoelectric response by assuming a simple functional form of the spectral conductivity was proposed by Mahan and Sofo [32] and was applied to various systems including the gapped Dirac cones [33]. Here, we apply this idea to the tilted Dirac cones. As we have seen, the spectral conductivity exhibits a dip for the type I and III Dirac cones. So, as the simplest approximation, we employ the following form of the spectral conductivity around the Dirac point,

$$\sigma(\epsilon) = \alpha_0 + \alpha_1 |\epsilon|, \tag{1.12}$$

where α_0 and α_1 are the constants. Substituting Eq. (1.12) into Eqs. (1.4), (1.5), and (1.11), and further considering the limit of $\alpha_0 \to 0$, we find that S and ZT can be given as

$$S = \frac{k_B}{e} \cdot \frac{h_2(-x) - 2xh_1(-x)}{2h_1(-x) - xh_0(-x)}, \tag{1.13}$$

and

$$ZT = \left\{ \frac{[2h_1(-x) - xh_0(-x)]\,[2h_3(-x) - xh_2(-x)]}{[h_2(-x) - 2xh_1(-x)]^2} - 1 \right\}^{-1}, \tag{1.14}$$

where $x = -\dfrac{\mu}{k_B T}$ and the functions $h_0 - h_3$ are given as

$$h_0(z) = \tanh \frac{z}{2}, \tag{1.15}$$

$$h_1(z) = \ln(1 + e^z) - \frac{ze^z}{e^z + 1}, \tag{1.16}$$

$$h_2(z) = \frac{2z^2 e^z}{e^z + 1} - 4z(1 + e^z) - 4\mathrm{Li}_2(-e^z) - \frac{\pi^2}{3}, \tag{1.17}$$

and

$$h_3(z) = z^2 \left[3\ln(1 + e^z) - \frac{ze^z}{e^z + 1} \right] + 6z\mathrm{Li}_2(-e^z) - 6\mathrm{Li}_3(-e^z). \tag{1.18}$$

Here, $\mathrm{Li}_n(z)$ stands for the polylogarithm function of order n. Notably, under this approximation, the Seebeck coefficient and the dimensionless figure of merit are functions of a single parameter, x, and they do not depend on the model-dependent parameter α_1.

Figure 1.6 shows the Seebeck coefficient and the dimensionless figure of merit as a function of $-x$. We see that the minimum of S is at $-x \sim 2$ $\left(\text{i.e., } T \sim \dfrac{\mu}{2\,k_B}\right)$, and the maximum of ZT is $-x \sim 2.5$ $\left(\text{i.e., } T \sim \dfrac{\mu}{2.5\,k_B}\right)$, which are in good agreement with

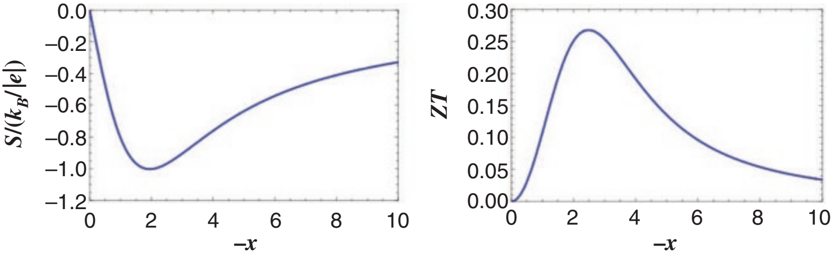

Figure 1.6 Seebeck coefficient (left) and the dimensionless figure of merit (right) as a function of $-x$ of Eqs. (1.13) and (1.14), respectively.

the numerical results for type I and III Dirac cones in Figure 1.5. We also see in Figure 1.6 that the maximal value of $|S|$ is about $k_B/|e| \sim 86\,\mu V/K$ and that of ZT is about 0.27. They are in the same order as the numerical results for the types I and III Dirac cones but do not agree at the quantitative level. This might be because of a non-negligible contribution arising from α_0 , whose value depends on the details of the model parameters and the damping rate.

To summarize this subsection, the microscopic theory based on Kubo–Luttinger formalism provides us with a powerful tool to investigate the thermoelectric transport arising from the characteristic dispersion relation of electrons in solids. In our analysis of the tilted Dirac-electron model, we have found that the optimal response is obtained for the type I Dirac cones with strongly tilted, rather than the type II and III Dirac cones. However, in the actual materials, the fine-tuning of the tilting and the chemical potential is not easy. This is the reason why composite materials such as multilayer systems have been attracting attention, as described in the next section.

1.3 Film-substrate Systems

Composite systems, consisting of multiple components shown in Figure 1.7a, have been of interest in the studies of the thermoelectric effects. The film-substrate systems are a typical example of composite systems as introduced in Figure 1.7b, and their thermoelectric effect has been studied extensively with the development of microfabrication technology.

In the film-substrate system, the Seebeck effect has been studied. More recently, the transverse thermoelectric effect such as the Nernst effect is focused on [6]. The film-substrate system of Fe–Ga alloy film and silicon substrate system shows the huge anomalous Nernst effect of 15 μV/K, which is larger than the bulk value of Fe–Ga alloy and that of Co_2MnGa, which is a record material [6]. The microscopic analysis of the thin-film and substrate system is very difficult, because the consideration of the electronic state and the treatment of the interfacial effect between film and substrate are complicated. Thus, in this section, we introduce the analysis method based on the circuit model [11].

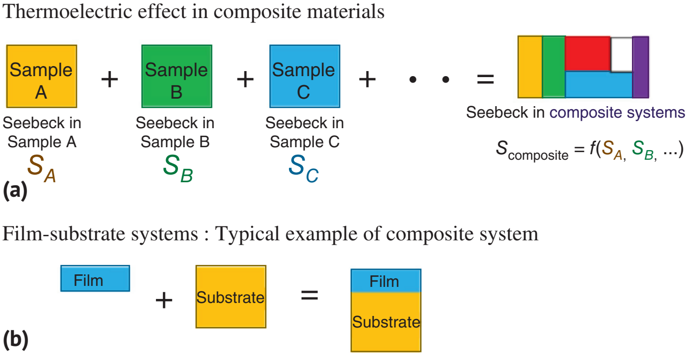

Figure 1.7 Schematic picture of a composite system. (a) Composite systems consisting of many components. (b) A thin-film substrate system as a typical example of a composite system.

1.3.1 Linear Response for Longitudinal and Transverse Thermoelectric Effects

Here, we describe the general linear response including not only the longitudinal but also the transverse thermoelectric effects [11]. When the external electrical and temperature gradients are applied to the x and y directions in system A, the electrical current density and heat current density along the x and y directions are given by

$$\begin{pmatrix} j_{e,A}^{x} \\ j_{e,A}^{y} \\ j_{Q,A}^{x} \\ j_{Q,A}^{y} \end{pmatrix} = \overline{L}_A \begin{pmatrix} E_{x,A} \\ E_{y,A} \\ -(\nabla T)_{x,A}/T \\ -(\nabla T)_{y,A}/T \end{pmatrix}, \tag{1.19}$$

where $j_{e,A}^{x(y)}$ and $j_{Q,A}^{x(y)}$ indicate the electric current and thermal current along $x(y)$ direction in system A, respectively, $E_{x(y),A}$ and $(\nabla T)_{x(y),A}$ are the external electric field and temperature gradient along the $x(y)$ direction in system A. $\overline{L}_A$ is a 4×4 matrix of linear response defined as

$$\overline{L}_A = \begin{pmatrix} L_{11,A}^{xx} & L_{11,A}^{xy} & L_{12,A}^{xx} & L_{12,A}^{xy} \\ L_{11,A}^{yx} & L_{11,A}^{yy} & L_{12,A}^{yx} & L_{12,A}^{yy} \\ L_{21,A}^{xx} & L_{21,A}^{xy} & L_{22,A}^{xx} & L_{22,A}^{xy} \\ L_{21,A}^{yx} & L_{21,A}^{yy} & L_{22,A}^{yx} & L_{22,A}^{yy} \end{pmatrix}. \tag{1.20}$$

Using the linear response coefficients, the Seebeck coefficient $(S_{xx,A})$, Nernst coefficient $(\nu_{yx,A})$, and anomalous Nernst coefficient $(N_{yx,A})$ are given as

$$S_{xx,A} = \frac{E_x}{(\nabla T)_x} = \frac{L_{12}^{xx}}{TL_{11}^{xx}}, \tag{1.21}$$

$$\nu_{yx,A} = \frac{E_{y,A}}{(\nabla T)_{x,A} B_z} = \frac{L_{11,A}^{xy} L_{12,A}^{xx} - L_{11,A}^{xx} L_{12,A}^{xy}}{TL_{11,A}^{xx} L_{11,A}^{yy} B_z}, \tag{1.22}$$

$$N_{yx,A} = \frac{E_{y,A}}{(\nabla T)_{x,A}} = \frac{L_{11,A}^{xy} L_{12,A}^{xx} - L_{11,A}^{xx} L_{12,A}^{xy}}{T\left(L_{11,A}^{xx} L_{11,A}^{yy} + \left(L_{11,A}^{xy}\right)^2\right)}. \tag{1.23}$$

1.3.2 Linear Response of Film-substrate System Based on the Circuit Model

Next, we derive the Seebeck coefficient, Nernst coefficient, and anomalous Nernst coefficient in film-substrate systems based on the circuit model [11]. Figure 1.8a shows the schematic picture of film-substrate systems. Here, we set a volume of film (substrate) as $a_x \times a_y \times d_{f(s)}$. As shown in Figure 1.8b, we treat the film-substrate systems as a parallel circuit consisting of film and substrate. Then, from Kirchhoff's law, the electrical potential of the film (substrate) along the $x(y)$ axis $\left(V_{x(y),f(s)}\right)$ satisfies the relation of

$$V_{x(y),f} = V_{x(y),s}. \tag{1.24}$$

where $V_{x(y),f(s)} = E_{x(y),f(s)} a_{x(y)}$.

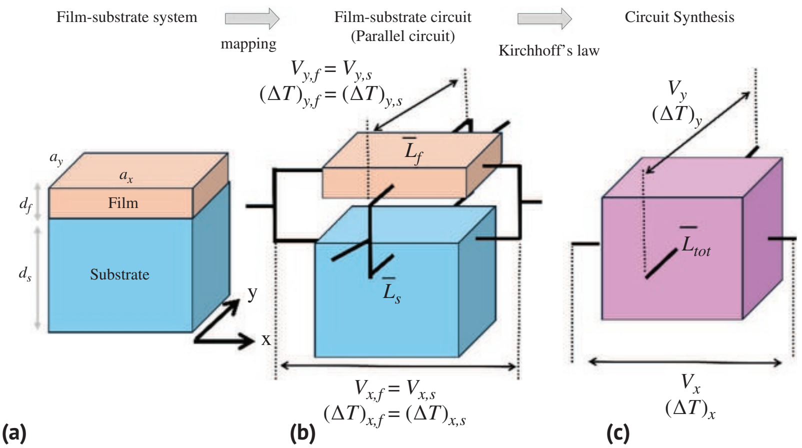

Figure 1.8 Schematic picture of (a) film-substrate system, (b) circuit model, and (c) circuit synthesis.

Next, we study the thermal circuit. Considering the temperature difference in a similar manner to the electric circuit, the temperature differences in film and substrate in the $x(y)$ axis also satisfy the following relation:

$$(\Delta T)_{x(y),f} = (\Delta T)_{x(y),s} \tag{1.25}$$

where $(\Delta T)_{x(y),f(s)} = (\nabla T)_{x(y),f(s)}\, a_{x(y)}$.

In the circuit model, the total of electric and thermal currents is given by the summation of those in the film and the substrate. Thus, the linear response coefficient of the synthesis circuit shown in Figure 1.8c is

$$\bar{L}_{\mathrm{tot}} = \frac{d_f}{d_f + d_s}\bar{L}_f + \frac{d_s}{d_f + d_s}\bar{L}_s. \tag{1.26}$$

Using Eq. (1.21), the Seebeck coefficient in the synthesis circuit is given by

$$S_{\mathrm{tot}} = \frac{S_f + \epsilon_\sigma S_s}{1 + \epsilon_\sigma}, \tag{1.27}$$

where

$$\epsilon_\sigma = \frac{L^{xx}_{11,s} d_s}{L^{xx}_{11,f} d_f} = \frac{L^{yy}_{11,s} d_s}{L^{yy}_{11,f} d_f} = \frac{R_f}{R_s}. \tag{1.28}$$

ϵ_σ corresponds to the ratio of the electric resistance of the film (R_f) and the substrate [5].

In the same manner, the Nernst coefficient and the anomalous Nernst coefficient are

$$\nu_{\mathrm{tot}} = \frac{\nu_f + \epsilon_\sigma \nu_s}{1 + \epsilon_\sigma} + \frac{\epsilon_\sigma}{(1 + \epsilon_\sigma)^2}\nu_s \delta\nu, \tag{1.29}$$

$$N_{\mathrm{tot}} = \frac{N_f + \epsilon_\sigma N_s}{1 + \epsilon_\sigma} + \frac{\epsilon_\sigma}{(1 + \epsilon_\sigma)^2} N_s \delta N, \tag{1.30}$$

where

$$\delta\nu = \left(S_f - S_s\right)\left(\theta_{H,s} - \theta_{H,f}\right)/\nu_s B_z, \tag{1.31}$$

$$\delta N = \left(S_f - S_s\right)\left(\theta_{H,s} - \theta_{H,f}\right)/N_s, \tag{1.32}$$

and $\theta_{H,f(s)}$ is the Hall angle of the film (substrate) defined as

$$\theta_{H,f(s)} = R_{H,f(s)} L^{xx}_{11,f(s)} B_z, \tag{1.33}$$

and the Hall coefficient of the film (substrate) $\left(R_{H,f(s)}\right)$ is

$$R_{H,f(s)} = \frac{L^{xy}_{11,f(s)}}{L^{xx}_{11,f(s)} L^{yy}_{11,f(s)} B_z}. \tag{1.34}$$

Noted that a similar expression of anomalous Nernst coefficient was derived in Ref. [6]. Based on the circuit model analysis, the thermoelectric effect of the film and substrate system is analyzed. It should be noted that the interfacial effect between the film and the substrate is not considered in this model.

1.3.3 Model Calculation

Finally, we show ϵ_σ dependence of Seebeck coefficient and Nernst coefficient using Eqs. (1.27) and (1.29). Figure 1.9 shows the ϵ_σ dependence of the Seebeck coefficient (black line) for $\frac{S_f}{S_s} = 100$ and the Nernst coefficient (red line) for $\frac{\nu_f}{\nu_s} = 10$ and $\delta\nu = 100$. The Seebeck coefficient gradually decreases as ϵ_σ increases. On the other hand, the Nernst coefficient exhibits a peak structure at $\epsilon_\sigma \simeq 1.0$. It should be noted that the anomalous Nernst effect behaves the same as the Nernst effect. The part of the Nernst effect in the second term of Eq. (1.29) means that the Nernst effect in the film (substrate) is derived from the Hall angle of the substrate (film). Thus, this is called the cooperative effect, which is a correlated effect between the film and the substrate [11].

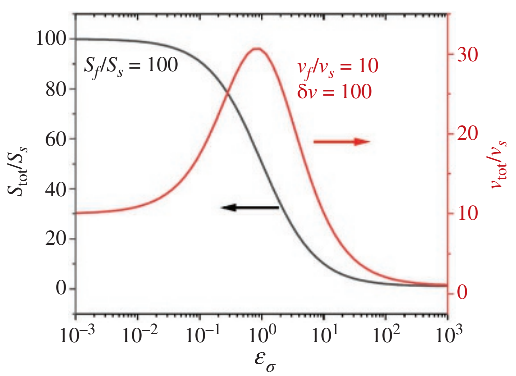

Figure 1.9 ϵ_σ dependence of Seebeck coefficient (black line) and Nernst coefficient (red line).

The peak structure was observed in Fe–Ga alloy film and silicon substrate system in the anomalous Nernst effect [6]. However, there are no experimental results in the Nernst effect, although there is a theoretical prediction in the Bi film and Si substrate system [11].

1.4 Summary

In this section, first, we introduced the microscopic theory of the thermoelectric effect based on the Kubo–Luttinger formalism and its application to the type I, II, and III Dirac systems, and then we show the analysis of film-substrate systems, which is a typical example of composite systems, by the circuit model. We expect that the combination of microscopic and macroscopic methods opens a new way to discover thermoelectric systems with high efficiency.

References

1. Nandihalli, N., Liu C.J. and Mori, T. (2020) Polymer based thermoelectric nanocomposite materials and devices: fabrication and characteristics. *Nano Energy*, 78, 105186.
2. Fu, C., Sun, Y. and Felser, C. (2020) Topological thermoelectrics. *APL Materials*, 8, 040913.
3. Bergman, D.J. and Levy, O. (1991) Thermoelectric properties of a composite medium. *J. Appl. Phys.*, 70, 6821.
4. Bergman, D.J. and Fel L.G. (1999) Enhancement of thermoelectric power factor in composite thermoelectrics. *J. Appl. Phys.*, 85, 8205.
5. Riss, A., Garmroudi, F., Parzer M., Pustogow A., Mori T., and Bauer E. (2024) Thermoelectric power factor of composites. *Phys. Rev. Appl.*, 21, 014002.
6. Zhou, W., Sasaki, T., Uchida, K.-I., and Sakuraba, Y. (2024) Direct-contact Seebeck-driven transverse magneto-thermoelectric generation in magnetic/thermoelectric bilayers. *Adv. Sci.*, 11, 2308543.
7. Kubo, R. (1957) Statistical-mechanical theory of irreversible processes. I. General theory and simple applications to magnetic and conduction problems. *J. Phys. Soc. Jpn.*, 12, 570.
8. Luttinger, J.M. (1964) Theory of thermal transport coefficients. *Phys. Rev.*, 135, A1505.
9. Ogata, M. and Fukuyama, H. (2019) Range of validity of Sommerfeld–Bethe relation associated with Seebeck coefficient and phonon drag contribution. *J. Phys. Soc. Jpn.*, 88, 074703.
10. Mizoguchi, T., Matsuura, H. and Ogata, M. (2022) Thermoelectric transport of type I, II, and III massless Dirac fermions in a two-dimensional lattice model. *Phys. Rev. B*, 105, 205203.
11. Matsuura, H., Riss, A., Garmroudi, F., Parzer, M., and Bauer, E. (2024) Cooperative Nernst effect of multilayer systems: parallel circuit model study. *Phys. Rev. Res.*, 6, 043071.

12 Sommerfeld, A. and Bethe, H. (1933) Elektronentheorie der Metalle, In H. Geiger and K. Scheel (Eds.), Handbuch der Physik, Vol. 24/2, Springer, Berlin/Heidelberg.

13 Yamamoto, T. and Fukuyama, H. (2018) Possible high thermoelectric power in semiconducting carbon nanotubes ∼a case study of doped one-dimensional semiconductors∼. *J. Phys. Soc. Jpn.*, 87, 024707.

14 Yamamoto, T. and Fukuyama, H. (2018) Bipolar thermoelectric effects in semiconducting carbon nanotubes: description in terms of one-dimensional dirac electrons. *J. Phys. Soc. Jpn.*, 87, 114710.

15 Matsubara, M., Sasaoka, K., Yamamoto, T., and Fukuyama, H. (2021) Optimal thermoelectric power factor of narrow-gap semiconducting carbon nanotubes with randomly substituted impurities. *J. Phys. Soc. Jpn.*, 90, 044702.

16 Horii, H., Matsubara, M., Sasaoka, K., Yamamoto, T., and Fukuyama, H. (2021) Optimization of thermoelectric power factor of bilayer graphene by vertical electric field. *J. Phys. Soc. Jpn.*, 90, 104711.

17 Hosoi, M., Tateishi, I., Matsuura, H., and Ogata, M. (2022) Thin films of topological nodal line semimetals as a candidate for efficient thermoelectric converters. *Phys. Rev. B*, 105, 085406.

18 Hirosawa, T., Schäfer, F., Maebashi, H., Matsuura, H., and Ogata, M. (2022) Data-driven reconstruction of spectral conductivity and chemical potential using thermoelectric transport properties. *J. Phys. Soc. Jpn.*, 91, 114603.

19 Endo, J., Matsuura, H. and Ogata, M. (2022) Effect of paramagnon drag on thermoelectric transport properties: linear response theory. *Phys. Rev. B*, 105, 045101.

20 Yamamoto, T., Ogata, M. and Fukuyama, H. (2022) Thermoelectric effect in Mott variable-range hopping. *J. Phys. Soc. Jpn.*, 91, 044704.

21 Matsubara, M., Yamamoto, T. and Fukuyama, H. (2023) Two-band model with high thermoelectric power factor and its application to FeSe thin film. *J. Phys. Soc. Jpn.*, 92, 104704.

22 Matsubara, M., Yamamoto, T. and Fukuyama, H. (2025) Sommerfeld–Bethe analysis of ZT in inhomogeneous thermoelectrics. *J. Phys. Soc. Jpn.*, 94, 024601.

23 Matsuura, H., Maebashi, H., Ogata, M., and Fukuyama, H. (2019) Effect of Phonon Drag on Seebeck Coefficient Based on Linear Response Theory: Application to $FeSb_2$. *J. Phys. Soc. Jpn.*, 88, 074601.

24 Fukuyama, H. and Ogata, M. (2020) Theory of phason drag effect on thermoelectricity. *Phys. Rev. B*, 102, 205136.

25 Endo, J., Matsuura, H. and Ogata, M. (2024) Phonon drag effect in Nernst and thermal Hall effects: general theory and application to dilute metal $SrTiO_{3-\delta}$. *Phys. Rev. B*, 110, 205121.

26 Matsuura, H., Ogata, M., Mori, T., and Bauer, E. (2021) Theory of huge thermoelectric effect based on a magnon drag mechanism: application to thin-film Heusler alloy. *Phys. Rev. B*, 104, 214421.

27 Takarada, S., Ogata, M. and Matsuura, H. (2021) Theory of thermal conductivity of excitonic insulators. *Phys. Rev. B*, 104, 165122.

28 Fuseya, Y., Ogata, M. and Fukuyama, H. (2015) Transport properties and diamagnetism of Dirac electrons in bismuth. *J. Phys. Soc. Jpn.*, 84, 012001.

29 Castro Neto, A.H., Guinea, F., Peres, N.M.R., Novoselov, K.S., and Geim, A.K. (2009) The electronic properties of graphene. *Rev. Mod. Phys.*, 81, 109.

30 Kajita, K., Nishio, Y., Tajima, N., Suzumura, Y., and Kobayashi, A. (2014) Molecular Dirac fermion systems - theoretical and experimental approaches-. *J. Phys. Soc. Jpn.*, 83, 072002.

31 Mizoguchi, T. and Hatsugai, Y. (2020) Type-III Dirac cones from degenerate directionally flat bands: viewpoint from molecular-orbital representation. *J. Phys. Soc. Jpn.*, 89, 103704.

32 Mahan, G.D. and Sofo, J.O. (1996) The best thermoelectric. *Proc. Natl. Acad. Sci. USA.*, 93, 7436.

33 Hasdeo, E.H., Krisna, L.P.A., Hanna, M.Y., Gunara, B.E., Hung, N.T., and Nugraha, A.R.T. (2019) Optimal band gap for improved thermoelectric performance of two-dimensional Dirac materials. *J. Appl. Phys.*, 126, 035109.